Inverse Transition Learning:
Learning Dynamics from Demonstrations

Leo Benac[1], **Abhishek Sharma**[1], **Sonali Parbhoo** [2], **Finale Doshi-Velez** [1]

[1]School of Engineering and Applied Sciences, Harvard University
[2]School of Electrical and Electronic Engineering, Imperial College London
lbenac@g.harvard.edu, abhisheksharma@g.harvard.edu, s.parbhoo@imperial.ac.uk, finale@seas.harvard.edu

Abstract

We consider the problem of estimating the transition dynamics T^* from near-optimal expert trajectories in the context of offline model-based reinforcement learning. We develop a novel constraint-based method, Inverse Transition Learning, that treats the limited coverage of the expert trajectories as a *feature*: we use the fact that the expert is near-optimal to inform our estimate of T^*. We integrate our constraints into a Bayesian approach. Across both synthetic environments and real healthcare scenarios like Intensive Care Unit (ICU) patient management in hypotension, we demonstrate not only significant improvements in decision-making, but that our posterior can inform when transfer will be successful.

Introduction

In traditional planning scenarios, the rewards R and transition dynamics T^* of the environment are known, and the goal is to compute the optimal policy π^* that maximizes long-term returns. However, in many real-world situations, the transition dynamics T^* are unknown. Model-Based Reinforcement Learning (MBRL) addresses this by first learning T^* and then performing planning, which improves data efficiency and enables counterfactual reasoning (Sutton and Barto 2018; Ghavamzadeh et al. 2015; Kidambi et al. 2020; Yu et al. 2021; Lee, Lee, and Kim 2021; Poupart et al. 2006; Ha and Schmidhuber 2018; Oh et al. 2015; Buesing et al. 2018).

This paper focuses on learning the true dynamics T^* in offline settings using batch data generated by a near-optimal expert. This is a common setting in fields like healthcare and education, where one can presume that the behavior policy is imperfect but generally reasonable. Learning T^* from observational data is challenging due to low coverage of the state-action space. Without the ability to interact with the environment, it is crucial to utilize the limited data effectively.

We leverage the knowledge that the trajectories are near-optimal to better estimate T^*. Consider the simple 2-state MDP shown on the next page. The blue path shows the observed optimal behavior leading to the goal state s_{goal} from s_1 after action a_1. The dashed lines represent the alternative hypothetical paths following an unobserved action a_2.

The fact that the expert chose action a_1 implies there must be a higher likelihood of reaching s_{goal} via a_1 than a_2 (i.e., $T^*(s_{\text{goal}}|s_1, a_1) > T^*(s_{\text{goal}}|s_1, a_2)$).

Observed expert: a_1
Unobserved: a_2
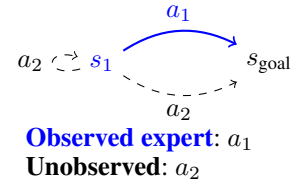
A popular definition of near-optimality models an expert's actions as being proportional to the action's values, as presented in Maximum Causal Entropy Inverse (MCE) RL (Ziebart, Bagnell, and Dey 2010).

In clinical settings, clinicians often prefer to administer treatments from drug families that have similar, reasonably good effects, without assigning a specific ranking. Conversely, they avoid poorly performing treatments, also without assigning a ranking. Instead of selecting a single best action, which may be influenced by data collection or other artifacts, it is often better to focus on sets of actions that are nearly equivalent in performance (Tang et al. 2020) and identify which poor behaviors to avoid (Fatemi et al. 2021; Tang et al. 2022; Rebello et al. 2023).

The most closely related works to ours (Herman et al. 2016; Reddy, Dragan, and Levine 2018) rely on the Maximum Causal Entropy (MCE) modeling approach. While modeling near-optimal expert behavior this way is reasonable, our modeling approach shows better performance in clinical settings. In addition, solving for T^* within the MCE framework requires a gradient-based procedure within an alternating optimization process, which is computationally intensive and prone to getting stuck in local optima. Additionally, the constraints used in these methods are soft, meaning their learned dynamics do not have any guarantees.

To address these limitations, we introduce a novel approach called *Inverse Transition Learning* (ITL), based on hard constraints on the true dynamics T^* and the distinction between the two groups of actions. Our constraints ensure that the values of executed actions exceed the values of actions not taken. If multiple actions are taken in the same state, they are constrained to be close in value. These thresholds are governed explicitly by a transparent and human-

understandable parameter, rather than implicitly through the entropy of an action-value distribution. They can also be solved for deterministically via a quadratic program (e.g., using CVXPY (Diamond and Boyd 2016)), avoiding the drawbacks of gradient-based optimization. This results in an optimization procedure that provides guarantees for the estimated dynamics and converges significantly faster.

The fact that the trajectories are near-optimal provides some information about what transition dynamics T^* are feasible, but limited coverage in the batch setting means that some uncertainty will still remain. Thus, we extend our approach to the Bayesian model-based setting (Dearden, Friedman, and Andre 2013). We develop an efficient approach to posterior estimation that includes our constraints. Our approach narrows the gap to the true dynamics T^* compared to baseline Bayesian MBRL methods. Additionally, given a new reward function, we demonstrate how keeping a posterior over the true dynamics T^* can be used to predict when the transfer will be successful. Our main contributions are:

- We propose a fast, transparent, and more reliable method to learn a point estimate of the true unknown dynamics T^* by leveraging expert demonstrations. Our method avoids gradient-based optimization, does not rely on the MCE modeling approach, and enforces constraint guarantees on the learned dynamics.

- We incorporate Bayesian inference to learn a posterior distribution over T^*. The posterior offers the same constraints guarantees for each sample, allows us to quantify the uncertainty over actions, and can be used to predict on which reward functions we except to perform well.

Although our method is designed for tabular MDPs, we demonstrate its effectiveness in continuous domains as well. We tested our approach in a range of environments, including a synthetic Gridworld, 10 different Randomworld environments, and a real-world healthcare setting. These experiments covered various levels of data coverage and expert optimality. Our results show that our method performs well across different metrics, consistently outpacing baseline methods in both synthetic and real-world scenarios.

Related Works

Model-Based Reinforcement Learning. We explore the utilization of forward models, which predict the subsequent state s' from the current state s and action a ($(s, a) \rightarrow s'$), as defined in (Moerland et al. 2023). These models are central for understanding action-induced state transitions. In contrast, backward models identify potential antecedents to states ($s' \rightarrow (s, a)$) and are used for backward planning (Moore and Atkeson 1993). Similarly, inverse models compute actions required to transition between states ($s, s' \rightarrow a$), beneficial in RRT planning (LaValle 1998). Additionally, non-parametric methods like replay buffers enable precise estimations (Lin 1992; Vanseijen and Sutton 2015; Van Hasselt, Hessel, and Aslanides 2019), and approximation methods, such as Gaussian processes, offer alternatives (Wang, Hertzmann, and Fleet 2005; Deisenroth and Rasmussen 2011). In discrete MDP settings like ours,

tabular maximum likelihood estimation models, noted as T^{MLE}, represent the state of the art (Sutton 1991).

Bayesian Model-Based Reinforcement Learning Bayesian MBRL integrates uncertainty into model learning, as detailed in the foundational works (Ghavamzadeh et al. 2015; Ross and Pineau 2008; Dearden, Friedman, and Andre 2013). Unlike previous approaches, such as (Poupart and Vlassis 2008) which address partially observable settings in discrete factored domains by updating beliefs based on new data, our method applies Bayesian MBRL in an offline setting. We infer posterior distributions over transition dynamics solely from expert knowledge. This approach utilizes prior knowledge and batch data to develop models that establish reliable policies (Guo, Yunfeng, and Geng 2022). In contrast, studies like (Zhang et al. 2020a,b) focus on learning invariant representations for control without explicitly modeling transition dynamics, which is a key aspect of our research.

Learning from Demonstrations. *Imitation Learning* (IL) involves learning policies directly from demonstrations by near-optimal experts using methods like training a policy at each timestep (Stéphane, Gordon Geoffrey, and Andrew 2010), DAgger (an iterative algorithm integrating expert feedback) (Ross, Gordon, and Bagnell 2011), and Approximate Policy Iteration with Demonstration (APID), which uses expert advice to impose linear constraints during policy optimization (Kim et al. 2013). These techniques primarily focus on behavioral cloning and policy learning. In contrast, *Inverse Reinforcement Learning* (IRL) seeks to learn the reward function R from the dynamics T and expert demonstrations, facilitating succinct task descriptions and transferability (Ng, Russell et al. 2000). Methods like Maximum Margin and Maximum Entropy IRL focus on deriving R to mimic expert policies robustly (Abbeel and Ng 2004; Ziebart et al. 2008; Scobee and Sastry 2019). Addressing R's non-identifiability, Bayesian IRL suggests learning a distribution over R, enhancing model adaptability (Ramachandran and Amir 2007). Distinct from these approaches, our work *Inverse Transition Learning* emphasizes learning the true dynamics T^*, a novel framework constructed to integrates expert demonstrations to refine the estimation of T^*. This method aims to understand and model the actual transitions within the environment, contrasting sharply with baseline methods that typically rely on maximum likelihood for estimation.

Preliminaries

Markov Decision Processes (MDPs). An MDP $\mathcal{M}$ can be represented as a tuple $\mathcal{M} = \{\mathcal{S}, \mathcal{A}, T^*, \gamma, R\}$, where $\mathcal{S}$ is the state space, $\mathcal{A}$ the action space, T^* is the true dynamics of the environment, γ is the discount factor and R is a bounded reward function. In planning, the goal is to find the best policy π^* corresponding to an MDP $\mathcal{M}$. In this paper, we focus on tabular MDPs (discrete state and action spaces). **Bellman Equations.** The values functions of a policy π are

given below:

$$V^\pi(s) = \mathbb{E}\left[\sum_{t=0}^\infty \gamma^t r_t \mid s_0 = s, \pi\right] \tag{1}$$

$$Q^\pi(s,a) = \mathbb{E}\left[\sum_{t=0}^\infty \gamma^t r_t \mid s_0 = s, a_0 = a, \pi\right] \tag{2}$$

Notation. Let $V^\pi \in \mathbb{R}^{|S|}$ denote the vector of values $V^\pi(s)$. We use shorthand $R_a \in \mathbb{R}^{|S|}$, $Q_a \in \mathbb{R}^{|S|}$, and $T_a \in \mathbb{R}^{|S| \times |S|}$ to represent the vectors $R(\cdot, a)$, $Q(\cdot, a)$ and the matrix $T(\cdot \mid \cdot, a)$. We also use shorthand R_π, Q_π, and T_π to represent the vectors $\mathbb{E}_{a \sim \pi}[R_a]$, $\mathbb{E}_{a \sim \pi}[Q_a]$ and the matrix $\mathbb{E}_{a \sim \pi}[T_a]$. For dynamics T, $\pi^*(T)$ denotes its corresponding optimal policy. In tabular settings, the value functions V^π and Q_a^π can be calculated directly through a closed-form solution:

$$V^\pi = R_\pi + \gamma T_\pi V^\pi = (I - \gamma T_\pi)^{-1} R_\pi \tag{3}$$

$$Q_a^\pi = R_a + \gamma T_a (I - \gamma T_\pi)^{-1} R_\pi. \tag{4}$$

Methods for Estimating the Transition Dynamics T^*. In tabular settings, a common method to estimate the true transition dynamics T^* is the Maximum Likelihood Estimate (MLE), denoted as T^{MLE} (e.g., (Barto, Bradtke, and Singh 1995; Kim and Oh 2023; Ornik and Topcu 2021)). The number of times the tuple (s, a, s') is observed is denoted by $N_{s,a,s'}$. We apply Laplace smoothing, represented by δ, to address issues such as zero occurrences in the count data due to low coverage in our batch data $\mathcal{D}$. The T^{MLE} is defined as:

$$T^{MLE}(s'|s,a) = \frac{N_{s,a,s'} + \delta}{\sum_{s'}(N_{s,a,s'} + \delta)} \tag{5}$$

In offline tabular settings, (Herman et al. 2016) leverage near-optimal batch data to infer dynamics by reusing the MCE IRL framework (Ziebart, Bagnell, and Dey 2010). We include this method in our baseline and refer to it as MCE (or T^{MCE}) moving forward. Their method consist of an interative procedure between taking one gradient step of the dynamics parameters θ with respect to the loss in equation 6 and then performing soft-Value Iteration, where Q is the soft Q function.

$$L_\theta^{MCE}(D) = \sum_{(s,a,s') \in D} \left[\log\left(\frac{\exp(Q_\theta(s,a))}{\sum_{a' \in \mathcal{A}} \exp(Q_\theta(s,a'))}\right) + \log T_\theta(s' \mid s, a)\right]. \tag{6}$$

To model the uncertainty of transitions T^* probabilistically, (Ghavamzadeh et al. 2015) utilizes a Multinomial likelihood function in conjunction with a Dirichlet prior. This combination yields the posterior distribution $P(T^*|\mathcal{D})$, which estimates the transition probabilities based on the observed data $\mathcal{D}$.

$$P(T^*(\cdot \mid s,a) \mid \mathcal{D}) = \text{Dir}(\mathbf{N}_{s,a} + \delta \mid s, a)$$
$$\propto \text{Multinomial}(\mathbf{N}_{s,a} \mid s, a) \cdot \text{Dir}(\delta \mid s, a) \tag{7}$$

Note that T^{MLE} represents the mean of the distribution $P(T^*|\mathcal{D})$. However, this posterior distribution is not as tight as it could be because it does not account for the near-optimality of expert trajectories. To refine this, we utilize expert signals to develop a tighter posterior $P(T^*|\mathcal{D})$, enhancing the estimation of the transition dynamics. To the best of our knowledge, we are the first to infer a distribution over the dynamics using expert demonstrations. Furthermore, we propose a method distinct from (Herman et al. 2016) to derive a point estimate of T^*. This involves formulating constraints based on expert behaviors, offering a more accurate approach to modeling the true dynamics.

Estimating Transition Dynamics with ϵ-optimal Expert

This section introduces key definitions to relate the expert's optimality to the true dynamics T^*. We describe the problem setting as follows:

Definition 1. (ϵ-ball) *For any state s and transition dynamics T, an action a is in the ϵ-ball $\epsilon(s;T)$ if it is ϵ-close to the optimal action according to the optimal Q-function $Q^*(.,.;T)$ (We refer to actions as **valid** if they are within the ϵ-ball for state s and dynamics T, and as **invalid** if they are outside this ϵ-ball):*

$$a \in \epsilon(s;T) \iff \max_{a'} Q^*(s,a';T) - Q^*(s,a;T) \le \epsilon$$

Definition 2. (ϵ-optimality) *A policy $\pi_\epsilon(.|s;T)$ is ϵ-optimal with respect to transition dynamics T if it exclusively selects actions from the ϵ-ball $\epsilon(s;T)$ for all states s. An action a is ϵ-optimal with respect to dynamics T if $a \in \epsilon(s;T)$.*

Definition 3. (ϵ-ball property) *Transition dynamics T satisfy the ϵ-ball property for state s if $\epsilon(s;T) = \epsilon(s;T^*)$ and all invalid actions are ϵ-away from all valid actions according to $Q^*(s,.;T)$.*

We aim to learn dynamics T that enforce the ϵ-ball property across all states s, ensuring that these dynamics can discern between valid and invalid actions.

Definition 4. (Deterministic/stochastic-policy state) *A deterministic-policy state occurs when the ϵ-optimal expert $\pi_\epsilon(.|s;T^*)$ selects a single action $a = a^*$ in state s. A stochastic-policy state occurs when the expert selects multiple possible actions in state s.*

Deterministic-policy states are akin to conditions well-understood by clinicians who are certain of the best treatment, whereas stochastic-policy states resemble conditions where multiple reasonable treatments are known without clear superiority.

Problem Setting We assume we are given the MDP $\mathcal{M}$ except for the true transition dynamics T^* (i.e., $\mathcal{M} \setminus \{T^*\}$). We also have access to batch data $\mathcal{D} = \{(s_i, a_i, s_i')\}_{i=1}^N$, where the data which is assumed to have been generated by the behavior policy $\pi_\epsilon(.|s;T^*)$, which is ϵ-optimal regarding the true dynamics T^*. Note that when $\epsilon = 0$, the expert $\pi_\epsilon(.|.;T^*)$ is fully optimal, and hence we would only encounter deterministic-policy states. As ϵ increases, the expert begins to act more suboptimally, leading to more stochastic-policy states.

Constraints on Transition Dynamics Given $\pi_\epsilon(.|.;T^*)$

In this section, we develop a set of constraints compatible with an ϵ-optimal expert with respect to the true unknown dynamics T^*. These constraints are designed to impose the desired structure when estimating the true dynamics T^* by enforcing the ϵ-ball property (3) for every state s (see Theorem 1). While the true transition dynamics T^* are unknown, we assume access to $\pi_\epsilon(.|.;T^*)$ for now but explain in and Algorithm 1 how to deal with the more realistic settings of having access to trajectories only. This allows us to determine $\epsilon(s;T^*)$ for each state s by examining the actions of $\pi_\epsilon(.|s;T^*)$ with non-zero probabilities. For a policy π, the constraints for each state s referred in this paper as **constraints(π)** are divided into two sets:

constraint 1(π): Differentiation Between Valid and Invalid Actions For every $a \in \epsilon(s;T^*)$ and every $a' \notin \epsilon(s;T^*)$:

$$Q^\pi(s,a;T) - Q^\pi(s,a';T) \geq \epsilon$$
$$\Longleftrightarrow$$
$$R(s,a) - R(s,a') + \gamma\left(T(\cdot \mid s,a) - T(\cdot \mid s,a')\right)^\top$$
$$\times (I - \gamma T_\pi)^{-1} R_\pi \geq \epsilon \quad (8)$$

This ensures that for every state s, *every* invalid action is at least ϵ-away from *every* valid action with respect to $Q^\pi(s,.;T)$.

constraint 2(π): ϵ-Closeness of Valid Actions For each distinct pair $(a,a') \in \epsilon(s;T^*)$, the absolute difference between their Q values is bounded by ϵ:

$$|Q^\pi(s,a;T) - Q^\pi(s,a';T)| \leq \epsilon$$
$$\Longleftrightarrow$$
$$\left| R(s,a) - R(s,a') + \gamma\left(T(\cdot \mid s,a) - T(\cdot \mid s,a')\right)^\top \right.$$
$$\left. \times (I - \gamma T_\pi)^{-1} R_\pi \right| \leq \epsilon \quad (9)$$

This ensures that for each state s, *every* action within the ϵ-ball under the true transition dynamics T^* is also ϵ-close under the transition dynamics T.

Theorem 1. *If $\pi_\epsilon(. \mid .;T^*) = \pi^*(T^*)$ and some dynamics T satisfies **constraints($\pi_\epsilon(. \mid .;T^*)$)** for each state s, then $\pi^*(T) = \pi^*(T^*)$. Hence, T will recover the optimal action a^* with respect to the true transition dynamics T^* for each state s. (Note that $\pi^*(T)$ refers to the optimal policy of dynamics T.)*

Proof. See Theorem 1 in the Appendix.

In general, given any deterministic policy π, we can utilize **constraints(π)** to recover a transition dynamics T such that $\pi^*(T) = \pi$, and thus recover dynamics T that explain the behavior induced by such policy π.

Lemma 1. *For any ϵ, if T satisfies **constraints($\pi^*(T)$)**, then T will satisfy the ϵ-ball property.*

Proof. See Lemma 1 in the Appendix.

Constraints on Transition Dynamics Given Batch Data $\mathcal{D}$ Only

In practical settings, direct access to the expert policy $\pi_\epsilon(\cdot|s;T^*)$ for each state s is typically unavailable, necessitating reliance on the batch data only $\mathcal{D}$, which might not cover all (state, action) pairs comprehensively. We construct an estimated policy, $\widehat{\pi}_\epsilon(\cdot|s;T^*)$, such that for $s \in \mathcal{D}$, $\widehat{\pi}_\epsilon(a|s;T^*)$ assigns a uniform probability to all actions a present in $\mathcal{D}$. For state $s \notin \mathcal{D}$, we determine the optimal action a using the proposed transition model T (looking at $\pi^*(T)$), and then assign this action a in the policy used to define constraints, as detailed in line 9 of Algorithm 1.

Methodology

In this section, we demonstrate how to leverage (near) optimal data with our constraints to infer both a point estimate and a posterior distribution over the true dynamics T^*, respectively referred to as *Inverse Transition Learning* (ITL) and *Bayesian Inverse Transition Learning* (BITL).

Inverse Transition Learning In Figure 4 of Appendix, we demonstrate the potential non-convexity of the feasible region arising from the constraints (Equations 8 and 9), attributed to the inverse operation on T. By substituting $T^{MLE}_{\widehat{\pi}_\epsilon(.|.;T^*)}$ for T in these constraints, we linearize them and transform the problem into a quadratic convex optimization problem, solved efficiently using CVXPY (Diamond and Boyd 2016). The optimization formulation is:

$$\min_T \sum_{(s,a,s')} N_{s,a,s'} \cdot \left[T(s' \mid s,a) - T^{MLE}(s' \mid s,a)\right]^2$$
$$\text{subject to} \quad \forall (s,a) \in \mathcal{D}, \forall a' \notin \epsilon(s;T^*):$$
$$R(s,a) - R(s,a') + \gamma\left(T(\cdot \mid s,a) - T(\cdot \mid s,a')\right)^\top$$
$$\times \left(I - \gamma T^{MLE}_{\widehat{\pi}_\epsilon(\cdot|\cdot;T^*)}\right)^{-1} R_{\widehat{\pi}_\epsilon(\cdot|\cdot;T^*)} \geq \epsilon,$$
$$\left| R(s,a) - R(s,a') + \gamma\left(T(\cdot \mid s,a) - T(\cdot \mid s,a')\right)^\top \right.$$
$$\left. \times \left(I - \gamma T^{MLE}_{\widehat{\pi}_\epsilon(\cdot|\cdot;T^*)}\right)^{-1} R_{\widehat{\pi}_\epsilon(\cdot|\cdot;T^*)} \right| \leq \epsilon \quad (10)$$

We denote the result of this optimization as $solve_{ITL}\left(\widehat{\pi}_\epsilon(.|.;T^*), T^{MLE}\right)$, where T^{MLE} is used to linearize the constraints. Linearizing the constraints with $T^{MLE}_{\widehat{\pi}_\epsilon(\cdot|\cdot;T^*)}$ is appropriate because it reflects the state-action space where we have data, and thus where we expect T^{MLE} to be accurate. This method not only accelerates training and provides guarantees on the constraints but also empirically outperforms (Herman et al. 2016), which relies on gradient descent and can be trapped in poor local optima, as shown in Table 4.

By iteratively solving the optimization problem as detailed in Algorithm 1, we obtain a point estimate $\widehat{T}^*$ that satisfies the ϵ-ball property for each state s in $\mathcal{D}$ (see Definition 3), aligning with the ϵ-optimal expert behavior ($\pi_\epsilon(.|.;T^*)$).

In essence, $\widehat{T}^*$ represents the dynamics that best fit the batch data $\mathcal{D}$ while also explaining the ϵ-optimal expert behavior induced by $\pi_\epsilon(.|.;T^*)$.

Algorithm 1: Point estimate $\widehat{T}^*$ (ITL)

1: $i \leftarrow 0$
2: $\pi^{(0)}(\cdot|s) \leftarrow \widehat{\pi}_\epsilon(\cdot|s; T^*)$ for $s \in \mathcal{D}$
3: $\pi^{(0)}(\cdot|s) \leftarrow$ uniform distribution for $s \notin \mathcal{D}$
4: $T^{(0)} \leftarrow T^{\text{MLE}}$
5: $T^{(1)} \leftarrow solve_{ITL}(\pi^{(0)}, T^{(0)})$
6: $i \leftarrow i + 1$
7: **while** $T^{(i)}$ does not satisfy ϵ-ball property for each $s \in \mathcal{D}$ **do**
8: $\quad \pi^{(i)}(\cdot|s) \leftarrow \widehat{\pi}_\epsilon(\cdot|s; T^*)$ for $s \in \mathcal{D}$
9: $\quad \pi^{(i)}(\cdot|s) \leftarrow \pi^*(T^{(i)})$ for $s \notin \mathcal{D}$
10: $\quad T^{(i+1)} \leftarrow solve_{ITL}(\{\pi^{(k)}, T^{(k)}\}_{k=0}^i)$
11: $\quad i \leftarrow i + 1$
12: **end while**

Algorithm 2: HMC with reflection for Bayesian ITL

1: First momentum half step
2: $m \leftarrow m - \frac{1}{2}\alpha\nabla E(w)$
3: **for** $l = 0$ to L **do**
4: $\quad$ Full spatial step
5: $\quad w \leftarrow w + \alpha m$
6: $\quad$ Transform w into T
7: $\quad T \leftarrow$ w_to_T(w)
8: $\quad$ Create $\widehat{\pi}_\epsilon(\cdot \mid \cdot; T^*)$ with proposed T
9: $\quad$ Squeeze maximum info
10: $\quad \pi \leftarrow \pi^*(T^{(i)})$
11: $\quad$ Check for **constraints**(π) (See)
12: $\quad$ **if** all **constraints**(π) satisfied **then**
13: $\quad\quad$ Full momentum step
14: $\quad\quad m \leftarrow m - \alpha\nabla E(w)$
15: $\quad$ **else**
16: $\quad\quad$ Bounce
17: $\quad\quad$ **constraints**(π) c is violated
18: $\quad\quad \hat{n} \leftarrow \nabla c(T)/\|\nabla c(T)\|$
19: $\quad\quad m \leftarrow m - 2(m \cdot \hat{n})\hat{n}$
20: $\quad$ **end if**
21: **end for**
22: Full spatial step
23: $w \leftarrow w + \alpha m$
24: Last momentum half step
25: $m \leftarrow m - \frac{1}{2}\alpha\nabla E(w)$

Bayesian Inverse Transition Learning Based on our constraints, we have demonstrated how to estimate the dynamics such that it aligns with an expert's behavior. However, both **constraint 1** and **constraint 2** (Inequality 8 and 9) lead to an underdetermined problem with infinitely many solutions. Instead of introducing a loss function as in optimization problem (10) and baseline MCE (Herman et al. 2016), we infer a posterior distribution on the true transition dynamics T^* to quantify such uncertainty. This approach also lets us apply the actual constraints to each sample directly, instead of approximating them through linearization as is done in point estimate setting. We introduce a sampling-based technique to infer this distribution, denoted as $P_\epsilon(T^*|\mathcal{D})$, assuming data is generated by an ϵ-optimal expert. We use our constraints to ensure each sample satisfies the ϵ-ball property for each state $s \in \mathcal{D}$.

Naive Approach: Rejection Sampling The complexity of deriving a posterior from expert trajectories with many constraints precludes an analytic solution. An initial attempt might involve drawing samples from the simpler $P(T^*|\mathcal{D})$ and rejecting those that fail to meet our constraints. This turns out to be very inefficient and rejects nearly all samples.

HMC with Reflection for ITL To enhance sampling efficiency within our constrained, high-dimensional space, we employ Hamiltonian Monte Carlo (HMC) with reflection ((Betancourt 2011)) (See 2). A more detailed version of the algorithm along with more details about inference can be find in the Algorithm 3 of the Appendix . This method involves transformations necessary for ensuring each sample lies within the Dirichlet simplex. If samples fail to meet **constraints 1 & 2** (8, 9) or exit the feasible region after the leap-frog integration, they are rejected. We start HMC with the point estimate $\widehat{T}^*$ that satisfies the ϵ-ball property (3) for observed states. This ensures necessary initial feasibility, leading to a rejection rate of about 20 to 60% using an adaptive step size, a marked improvement over nearly 100% rejection in rejection sampling.

Experimental Setup

Environments Our evaluations span 11 synthetic environments and a real-life ICU setting. Specifically, we use a 25 states Gridworld with four actions, 10 different 15-states Randomworld with five actions each, and a healthcare scenario focusing on ICU patients with hypotension, utilizing the MIMIC-IV dataset (Johnson et al. 2020). In Gridworld, we generate 100 batches of data $\mathcal{D}$, each consisting of five episodes with 15 steps each. For each 10 of the Randomworld, 50 batches are generated, each containing three episodes of ten steps, due to their smaller size. We also evaluate our methods across varying "Coverage %" levels in these environments, defined as the percentage of states observed within each batch data $\mathcal{D}$ and various ϵ values to see how our method compare to baselines for various degrees of sub-optimality. Detailed descriptions of both the synthetic and real-world environments are available in the Appendix.

In synthetic scenarios, we simulate a suboptimal expert, where approximately 40% of states are stochastic-policy states (See definition 4), demonstrating the robustness of our approach to suboptimal expert behavior. We also include in the Appendix (Table 5, 6, Figure 6 and 7), results for 20% and 0% (fully optimal expert) of stochastic-policy states which correspond to lower ϵ values. Note that increased optimality from the expert (lower ϵ values) leads to less stochasticity (ie. less stochastic-policy states) amongst the actions selected in the batch data $\mathcal{D}$. Our method does not require the expert to be perfectly optimal and can adapt to various degrees of optimality through ϵ. In the results below, we use $\gamma = 0.95$ and smoothing parameter defined in Equation 5

$\delta = 0.001$.

Baselines. Our methods, Bayesian Inverse Transition Learning (BITL) and Inverse Transition Learning (ITL), are evaluated against T^{MLE} (Maximum Likelihood Estimation, MLE), T^{MCE} (Maximum Causal Entropy, MCE) (Herman et al. 2016), and a non-expert-informed posterior $P(T^*|\mathcal{D})$ (Posterior Sampling, PS).

Metrics. We use the following metrics to evaluate learnt dynamics $T's$ and induced policies $\pi's$:

Best/ϵ-ball action matching: Proportion of states where the best/ϵ-good action taken:

$$\frac{1}{|\mathcal{S}|}\sum_{s\in\mathcal{S}}\mathcal{I}\{\arg\max_a \pi(a|s) = \arg\max_a \pi^*(a|s)\}\Big/$$

$$\frac{1}{|\mathcal{S}|}\sum_{s\in\mathcal{S}}\mathcal{I}\{\arg\max_a \pi(a|s) \in \epsilon(s; T^*)\}$$

Bayesian regret: Regret of a sample-based empirical posterior distribution $\widehat{P}(T|\mathcal{D})$, where $|\widehat{P}(T|\mathcal{D})|$ is number of T's in the sample-based distribution:

$$\frac{1}{|\widehat{P}(T|\mathcal{D})|^2}\sum_{T\in\widehat{P}(T|\mathcal{D})}\sum_{T'\in\widehat{P}(T|\mathcal{D})}$$

$$\mathbb{E}_{s_0\sim\mu_0}\left[\left|V^{\pi^*(T)}(s_0; T) - V^{\pi^*(T')}(s_0; T)\right|\right]$$

We also report the normalized **Value**, calculated as the ratio of the value achieved by the optimal policy of our learned dynamics under the true dynamics T^* to the expected value under the true dynamics $\mathbb{E}_{s_0}[V^*(s_0; T^*)]$. Finally, we report the **CVaR** of Value over datasets, **Total Variation**, the **number of our constraints (8, 9) violated**, and the training **Time**(in seconds) for the baseline MCE and our method ITL. **Value** and **Best/ϵ-ball action matching** metrics are computed both in standard and transfer settings. In this paper, a transfer task refers to the evaluation of the learned dynamics and/or policy under a reward function different from the one used during training. To demonstrate that our learned dynamics can adapt to actions not seen in the demonstrations, we set up a transfer task where the optimal actions under this new reward function differ from those in the original task (See Figure 5, 6). This ensures the new task requires actions we didn't observe in the initial demonstrations. This tests the model's adaptability to changes in task conditions.

Computing the results. For each dynamics T, we compute its optimal policy $\pi^*(T)$ using Value Iteration (Sutton and Barto 2018), when needed to compute a metrics in terms of policies. For posterior distributions $P(T|\mathcal{D})$ and $P_\epsilon(T|\mathcal{D})$, we determine the optimal policies of 5,000 sampled $T's$ and average them.

How to Tune ϵ: In the healthcare setting, we only have access to an offline dataset. To select an appropriate ϵ, we evaluate the performance of ITL on a held-out validation set. We choose the ϵ that performs best on this validation set based on the **Best/ϵ-ball action matching metric** for both standard and transfer tasks (defined by different reward functions). As shown in Figure 1, $\epsilon = 5$ appears to be suitable, and this value is used for training and computing the
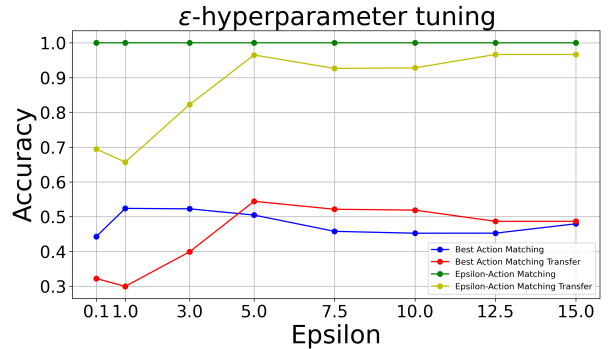
Figure 1: Performance of ITL on a held out validation set across different ϵ values.

results in the healthcare experiments (See Table 1). We also present results for $\epsilon = 10$ and $\epsilon = 15$, as these values are also reasonable. Results for $\epsilon = 10$ and $\epsilon = 15$ are provided in Tables 7 and 8 in the Appendix, showing similar performance.

Results

ITL consistently outperforms baseline methods across all metrics and coverage settings. Table 4, Table 1 and Figure 2 show that ITL and BITL outperform other baselines across different metrics and coverage levels, in both synthetic environments and the real-life healthcare environment. In Randomworlds, BITL and ITL significantly surpass MCE, which outperforms MLE and PS. In Gridworld, ITL slightly outperforms MCE on average but exhibits significantly better worst-case performance. This highlights the importance of inferring dynamics that satisfy hard constraints and the potential of MCE to get stuck in bad local optima due to gradient-based optimization. ITL also takes significantly less time to train. BITL outperforms all methods, showing that modeling uncertainty over dynamics while leveraging expert demonstrations can help outperform point estimate methods. In the standard task setting, as Theorem 1 guarantees, ITL and BITL are the only methods converging to optimal as coverage increases (left column of Figure 2). They achieve higher values without violating constraints, attributed to enforcing hard constraints in our work versus soft constraints in MCE.

ITL enables reliable, fast, and data-efficient dynamics estimation. In Gridworld, MCE required significantly more training time than ITL (137 seconds vs. 1 second) and showed poorer CVaR values, highlighting the challenges of gradient optimization in non-convex settings. ITL's efficiency is also evident in Randomworld, with training times of 0.70 seconds compared to MCE's 35 seconds (See Table 4). Our methods consistently converge to optimal performance as coverage increases, demonstrating consitency with expert demonstrations. MCE's tendency to get trapped in local optima underscores the efficiency and reliability of ITL and BITL in complex environments.

The policies from our method stay in the support of
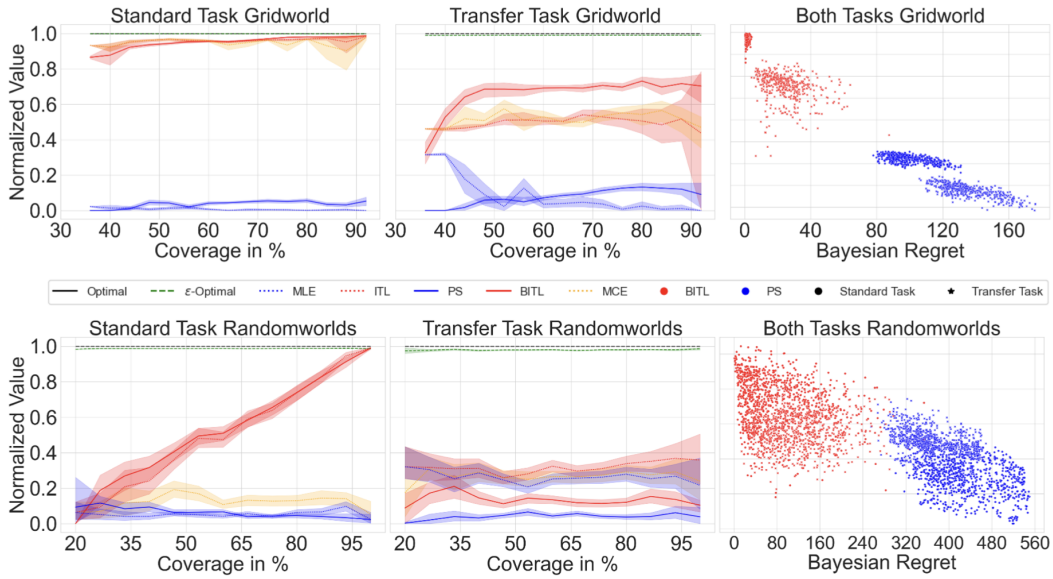
Figure 2: Top row: Normalized Value vs. Coverage for Gridworld (left: Standard Task, middle: Transfer Task), Bottom row: Normalized Value vs. Coverage for Randomworlds (left: Standard Task, middle: Transfer Task). Rightmost plots: Normalized Value vs. Bayesian Regret of both Tasks (top: Gridworld, bottom: Randomworlds).

Table 1: Healthcare dataset results environment ($\epsilon = 5$)

	Standard Task					Transfer Task				
Method	**MLE**	ITL	MCE	BITL	PS	MLE	ITL	MCE	BITL	PS
Best matching	0.33	**0.51**	0.31	0.49	0.31	0.34	**0.52**	0.32	0.47	0.34
ϵ matching	0.52	**1**	0.56	**1**	0.51	0.58	**0.97**	0.68	0.90	0.58
Nbr Constraints	61	**0**	47	**0**	58	-	-	-	-	-
Time	-	**2.23**	118	-	-	-	-	-	-	-
Bayesian Regret	-	-	-	**2.49**	10	-	-	-	**2.80**	5.40
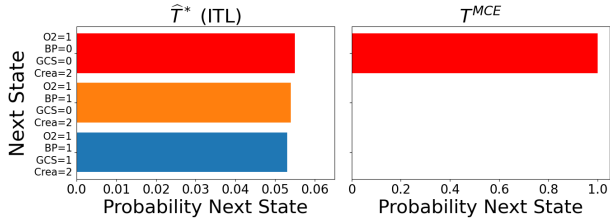
Figure 3: Most likely next 3 states after prescribing Intravenous treatment in state O2= 1, BP = 1, GCS = 1, Crea = 2

the expert's actions in *every* visited state, by imposing hard constraints leading to better worst case scenarios. Our methodology enforces hard constraints, ensuring policies adhere to expert actions in every visited state, thus recovering an ϵ-optimal action for each state and minimizing constraint violations. Unlike MLE, PS, and MCE, which occasionally breach constraints (See Table 4 and Table 1), ITL and BITL maintain strict compliance, enhancing reliability. CVaR results in Table 4 show ITL and BITL provide better worst-case outcomes by enforcing ϵ-ball property on the estimated dynamics (See Definition 3), preserving policy

robustness, even in challenging scenarios.

Our method integrates efficiently with Bayesian inference, useful for settings requiring more exploration and for predicting when we can transfer well Our integration with Bayesian inference enables us to infer calibrated uncertainties effectively, leveraging expert knowledge to enhance performance, particularly in environments like Gridworld where exploration avoid repeated suboptimal decisions such as repeatedly colliding with a wall due to poor action choices. This problem is less pronounced in Randomworld, illustrating the adaptability of our approach to different dynamics. Furthermore, the Bayesian framework allows us to predict with greater accuracy which tasks will likely yield successful outcomes based on the learned distributions. Looking at the Regrets plots (right column of Figure 2), we observe a clear correlations between the Bayesian Regret values and how well we perform on a task. The plot clearly show higher regret for the transfer task compared to the standard task which makes sense. In table 1, we show how similar reasoning can be applied to a real-life dataset where we see that we clearly perform better on task which lower regret.

Our method can be used into a continous real-life

healthcare settings and provides insights through counterfactual reasoning. In the healthcare environment, we discretize the state space based on the following feature values: Oxygen ratio (O2), Blood pressure (BP), Creatinine (Crea), and Glasgow Coma Scale (GCS). Details on the discretization rules are provided in Table 2 of the Appendix. After prescribing intravenous treatment under the current state (O2 = 1, BP = 1, GCS = 1, Crea = 2), we examine the three most likely subsequent states for the MLE, ITL, and MCE methods. Intravenous treatment is expected to improve blood pressure and creatinine levels. Since clinicians never prescribed intravenous treatment in this state, MLE results are uniform across all states and omitted from the plots. ITL shows that the likelihood of the next states is distributed among states that either improve blood pressure, creatinine, or remain the same. In contrast, MCE assigns all its likelihood to a single state, which is unrealistic given the complexities of human physiology and the lack of observed transitions. This example highlights how the MCE framework can produce unrealistic results in complex real-life settings. It is important to note that for ITL, the probability of the next states in Figure 3 is close to uniform quantitatively. This is due to the fact that we are using a uniform prior and have not observed any data for that state. However, our method can rank and hence quantify the uncertainty over the next states in a more informed way than MLE (which is exactly uniform) or MCE, which reduces its uncertainty to 0 even when no data exists for that particular state.

Discussion

Summary We tackled the challenge of estimating transition dynamics T^* from near-optimal expert trajectories in offline model-based reinforcement learning. Our approach, Inverse Transition Learning (ITL), leverages the limited coverage of expert trajectories and the near-optimality of the expert to estimate T^*. We introduced a novel constraint-based method and integrated these constraints within a Bayesian framework to learn a posterior distribution over the dynamics. To our knowledge, this is the first method to combine posterior estimation of dynamics with expert demonstrations. Our approach significantly enhances decision-making in both synthetic environments and real-world healthcare scenarios, such as ICU patient management for hypotension. It not only improves decision quality but also offers insights into the likelihood of successful task transfer, showcasing the robustness and adaptability of our method.

Future Work While our method provides a robust approach for estimating environmental dynamics using expert demonstrations, it is currently limited to discrete and fully observable state spaces. Future research could explore extending ITL to handle more complex environments, including those with high-dimensional, continuous, or partially observable state spaces. Additionally, combining ITL with Inverse Reinforcement Learning (IRL) to simultaneously learn rewards and dynamics represents another promising avenue for future work.

References

Abbeel, P.; and Ng, A. Y. 2004. Apprenticeship learning via inverse reinforcement learning. In *Proceedings of the twenty-first international conference on Machine learning*, 1.

Barto, A. G.; Bradtke, S. J.; and Singh, S. P. 1995. Learning to act using real-time dynamic programming. *Artificial intelligence*, 72(1-2): 81–138.

Betancourt, M. 2011. Nested sampling with constrained hamiltonian monte carlo. In *AIP Conference Proceedings*, volume 1305, 165–172. American Institute of Physics.

Betancourt, M. 2012. Cruising the simplex: Hamiltonian Monte Carlo and the Dirichlet distribution. In *AIP Conference Proceedings 31st*, volume 1443, 157–164. American Institute of Physics.

Buesing, L.; Weber, T.; Zwols, Y.; Racaniere, S.; Guez, A.; Lespiau, J.-B.; and Heess, N. 2018. Woulda, coulda, shoulda: Counterfactually-guided policy search. *arXiv preprint arXiv:1811.06272*.

Dearden, R.; Friedman, N.; and Andre, D. 2013. Model-based Bayesian exploration. *arXiv preprint arXiv:1301.6690*.

Deisenroth, M.; and Rasmussen, C. E. 2011. PILCO: A model-based and data-efficient approach to policy search. In *Proceedings of the 28th International Conference on machine learning (ICML-11)*, 465–472.

Diamond, S.; and Boyd, S. 2016. CVXPY: A Python-embedded modeling language for convex optimization. *The Journal of Machine Learning Research*, 17(1): 2909–2913.

Fatemi, M.; Killian, T. W.; Subramanian, J.; and Ghassemi, M. 2021. Medical dead-ends and learning to identify high-risk states and treatments. *Advances in Neural Information Processing Systems*, 34: 4856–4870.

Ghavamzadeh, M.; Mannor, S.; Pineau, J.; Tamar, A.; et al. 2015. Bayesian reinforcement learning: A survey. *Foundations and Trends® in Machine Learning*, 8(5-6): 359–483.

Guo, K.; Yunfeng, S.; and Geng, Y. 2022. Model-based offline reinforcement learning with pessimism-modulated dynamics belief. *Advances in Neural Information Processing Systems*, 35: 449–461.

Ha, D.; and Schmidhuber, J. 2018. Recurrent world models facilitate policy evolution. *Advances in neural information processing systems*, 31.

Herman, M.; Gindele, T.; Wagner, J.; Schmitt, F.; and Burgard, W. 2016. Inverse reinforcement learning with simultaneous estimation of rewards and dynamics. In *Artificial intelligence and statistics*, 102–110. PMLR.

Jiang, N.; Kulesza, A.; Singh, S.; and Lewis, R. 2015. The dependence of effective planning horizon on model accuracy. In *Proceedings of the 2015 International Conference on Autonomous Agents and Multiagent Systems*, 1181–1189.

Johnson, A.; Bulgarelli, L.; Pollard, T.; Horng, S.; Celi, L. A.; and Mark, R. 2020. Mimic-iv. *PhysioNet. Available online at: https://physionet. org/content/mimic-civ/1.0/(accessed August 23, 2021)*.

Kidambi, R.; Rajeswaran, A.; Netrapalli, P.; and Joachims, T. 2020. Morel: Model-based offline reinforcement learning. *Advances in neural information processing systems*, 33: 21810–21823.

Kim, B.; Farahmand, A.-m.; Pineau, J.; and Precup, D. 2013. Learning from limited demonstrations. *Advances in Neural Information Processing Systems*, 26.

Kim, B.; and Oh, M.-h. 2023. Model-based offline reinforcement learning with count-based conservatism. In *International Conference on Machine Learning*, 16728–16746. PMLR.

LaValle, S. 1998. Rapidly-exploring random trees: A new tool for path planning. *Research Report 9811*.

Lee, B. J.; Lee, J.; and Kim, K. E. 2021. Representation balancing offline model-based reinforcement learning. In *9th International Conference on Learning Representations, ICLR 2021*.

Lin, L.-J. 1992. Self-improving reactive agents based on reinforcement learning, planning and teaching. *Machine learning*, 8: 293–321.

Moerland, T. M.; Broekens, J.; Plaat, A.; Jonker, C. M.; et al. 2023. Model-based reinforcement learning: A survey. *Foundations and Trends® in Machine Learning*, 16(1): 1–118.

Moore, A. W.; and Atkeson, C. G. 1993. Prioritized sweeping: Reinforcement learning with less data and less time. *Machine learning*, 13: 103–130.

Ng, A. Y.; Russell, S.; et al. 2000. Algorithms for inverse reinforcement learning. In *Icml*, volume 1, 2.

Oh, J.; Guo, X.; Lee, H.; Lewis, R. L.; and Singh, S. 2015. Action-conditional video prediction using deep networks in atari games. *Advances in neural information processing systems*, 28.

Ornik, M.; and Topcu, U. 2021. Learning and planning for time-varying mdps using maximum likelihood estimation. *The Journal of Machine Learning Research*, 22(1): 1656–1695.

Poupart, P.; and Vlassis, N. 2008. Model-based Bayesian reinforcement learning in partially observable domains. In *Proc Int. Symp. on Artificial Intelligence and Mathematics,*, 1–2.

Poupart, P.; Vlassis, N.; Hoey, J.; and Regan, K. 2006. An analytic solution to discrete Bayesian reinforcement learning. In *Proceedings of the 23rd international conference on Machine learning*, 697–704.

Ramachandran, D.; and Amir, E. 2007. Bayesian Inverse Reinforcement Learning. In *IJCAI*, volume 7, 2586–2591.

Rebello, A.; Tang, S.; Wiens, J.; and Parbhoo, S. 2023. Leveraging Factored Action Spaces for Off-Policy Evaluation. *arXiv preprint arXiv:2307.07014*.

Reddy, S.; Dragan, A.; and Levine, S. 2018. Where do you think you're going?: Inferring beliefs about dynamics from behavior. *Advances in Neural Information Processing Systems*, 31.

Ross, S.; Gordon, G.; and Bagnell, D. 2011. A reduction of imitation learning and structured prediction to no-regret online learning. In *Proceedings of the fourteenth international conference on artificial intelligence and statistics*, 627–635. JMLR Workshop and Conference Proceedings.

Ross, S.; and Pineau, J. 2008. Model-based Bayesian reinforcement learning in large structured domains. In *Uncertainty in artificial intelligence: proceedings of the... conference. Conference on Uncertainty in Artificial Intelligence*, volume 2008, 476. NIH Public Access.

Scobee, D. R.; and Sastry, S. S. 2019. Maximum likelihood constraint inference for inverse reinforcement learning. *arXiv preprint arXiv:1909.05477*.

Stéphane, R.; Gordon Geoffrey, J.; and Andrew, B. J. 2010. No-regret reductions for imitation learning and structured prediction. *arXiv preprint arXiv: 1011.0686*.

Sutton, R. S. 1991. Dyna, an integrated architecture for learning, planning, and reacting. *ACM Sigart Bulletin*, 2(4): 160–163.

Sutton, R. S.; and Barto, A. G. 2018. *Reinforcement learning: An introduction*. MIT press.

Tang, S.; Makar, M.; Sjoding, M.; Doshi-Velez, F.; and Wiens, J. 2022. Leveraging factored action spaces for efficient offline reinforcement learning in healthcare. *Advances in Neural Information Processing Systems*, 35: 34272–34286.

Tang, S.; Modi, A.; Sjoding, M.; and Wiens, J. 2020. Clinician-in-the-loop decision making: Reinforcement learning with near-optimal set-valued policies. In *International Conference on Machine Learning*, 9387–9396. PMLR.

Van Hasselt, H. P.; Hessel, M.; and Aslanides, J. 2019. When to use parametric models in reinforcement learning? *Advances in Neural Information Processing Systems*, 32.

Vanseijen, H.; and Sutton, R. 2015. A deeper look at planning as learning from replay. In *International conference on machine learning*, 2314–2322. PMLR.

Wang, J.; Hertzmann, A.; and Fleet, D. J. 2005. Gaussian process dynamical models. *Advances in neural information processing systems*, 18.

Yu, T.; Kumar, A.; Rafailov, R.; Rajeswaran, A.; Levine, S.; and Finn, C. 2021. Combo: Conservative offline model-based policy optimization. *Advances in neural information processing systems*, 34: 28954–28967.

Zhang, A.; Lyle, C.; Sodhani, S.; Filos, A.; Kwiatkowska, M.; Pineau, J.; Gal, Y.; and Precup, D. 2020a. Invariant causal prediction for block mdps. In *International Conference on Machine Learning*, 11214–11224. PMLR.

Zhang, A.; McAllister, R.; Calandra, R.; Gal, Y.; and Levine, S. 2020b. Learning invariant representations for reinforcement learning without reconstruction. *arXiv preprint arXiv:2006.10742*.

Ziebart, B. D.; Bagnell, J. A.; and Dey, A. K. 2010. Modeling interaction via the principle of maximum causal entropy. In *Proceedings of the 27th International Conference on International Conference on Machine Learning*, 1255–1262.

Ziebart, B. D.; Maas, A. L.; Bagnell, J. A.; Dey, A. K.; et al. 2008. Maximum entropy inverse reinforcement learning. In *Aaai*, volume 8, 1433–1438. Chicago, IL, USA.

Proofs

Theorem 1. *If $\pi_\epsilon(.|.;T^*) = \pi^*(T^*)$ and some dynamics T satisfies **constraints**$(\pi_\epsilon(.|.;T^*))$ for each state s, then $\pi^*(T) = \pi^*(T^*)$. Hence, T will recover the optimal action a^* with respect to the true transition dynamics T^* for each state s.*

Proof. Since $\pi_\epsilon(.|.;T^*) = \pi^*(T^*)$, for each state s: $\epsilon(s;T^*) = \{a^*\} = \{\pi^*(T^*)(s)\}$. Hence, **constraints**$(\pi_\epsilon(.|.;T^*)) = $ **constraints**$(\pi^*(T^*))$ implies that for all $a' \in \mathcal{A}$, $a' \neq a^*$, T will satisfies:

$$Q^{\pi^*(T^*)}(s,a^*;T) - Q^{\pi^*(T^*)}(s,a';T) \geq \epsilon$$
$$\implies Q^{\pi^*(T^*)}(s,a^*;T) \geq Q^{\pi^*(T^*)}(s,a';T),$$

Thus, the transition dynamics T will favor the same action a^* as the true transition dynamics T^* for each state s. So if we attempt policy improvement on $Q^{\pi^*(T^*)}(s,.;T)$, we will end up with the same policy $\pi^*(T^*)$, meaning $\pi^*(T) = \pi^*(T^*)$ is the optimal policy for dynamics T.

Lemma 1. *For any ϵ, if T satisfies **constraints**$(\pi^*(T))$, then T will satisfies the ϵ-ball property.*

Proof. For each state s, **Constraint 1**$(\pi^*(T))$ and Theorem 1 imply $\pi^*(T)(s) \in \epsilon(s;T^*)$ because $Q^*(s,a;T)$ is greater than $Q^*(s,a';T) + \epsilon$ for all $a \in \epsilon(s;T^*)$ and $a' \notin \epsilon(s;T^*)$. This ensures that *every* invalid action is ϵ-away from *every* valid action under the dynamics T. Additionally, **Constraint 2**$(\pi^*(T))$ guarantees that $\epsilon(s;T^*) = \epsilon(s;T)$ by ensuring that for each valid action $a \in \epsilon(s;T^*)$, the $\max_{a'} Q^*(s,a';T) - Q^*(s,a;T) \leq \epsilon$. This completes the proof that the dynamics T satisfy the ϵ-ball property.

Non-Convex Feasible Region

When plotting our constraints (equations 8 and 9) within a three-dimensional subspace of a toy example, as illustrated in Figure 4, it becomes apparent that the feasible region can be non-convex, primarily due to the inverse operations within the constraints.

Inference Details

HMC for Dirichlet

The log-likelihood function of the target distribution takes the following form:

$$\log P(T^*|D) = \sum_{s,a} Dir(\mathbf{N}_{s,a} + \delta|s,a) \tag{11}$$

Applying HMC to Dirichlet distributions is challenging due to the constrained nature of these distributions, which can hinder the efficiency of standard HMC methods. To address these issues, (Betancourt 2012) introduce a set of invertible transformations that reshape the Dirichlet distribution into a more tractable form by removing the simplex constraints of the original Dirichlet. To make our sampling more efficient in high dimensional settings, we add a logit transformation to remove the need of the Dirichlet variables
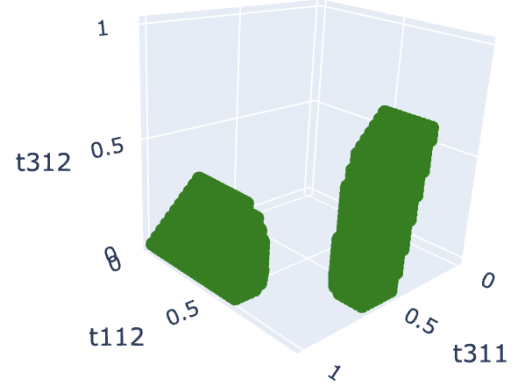
Figure 4: Example of a subspace of the feasible region defined by the constraints on T. The label 'tsas'' indicates the probability of transitioning to state s' after being in state s and taking action a.

to be in between 0 and 1. We will refer as w as the variable obtained after applying all of these transformations on a transition dynamics T. Since all of the transformations are invertible we can easily go from one variable to the other. Algorithm 2 summarize how to sample from $P_\epsilon(T^*|\mathcal{D})$. We based our algorithm based on the first order leapfrog with constraint HMC algorithm of (Betancourt 2011).

HMC for Dirichlet with Reflection

Notation

- m: The momentum variable, representing the current momentum.
- w: The position variable, denoting the current position.
- T: Corresponding transition dynamics of the position variable w
- α: The step size parameter, which determines the scale of each discrete step in the leapfrog integration.
- $\nabla E(w)$: The gradient of the energy function at position w, used to compute the force in the Hamiltonian dynamics.
- $C(T)$: All the constraints function that ensures the trajectory remains within the valid region defined by our constraints in terms of the dynamics T.
- L: The total number of integration steps to be performed in the leapfrog algorithm.
- l: An index variable representing the current time step within the loop of the leapfrog integration.
- w_to_T Transform variable w into variable T. (See (Betancourt 2012))
- T_to_w Transform variable T into variable w. (See (Betancourt 2012))

Note that if after the final leap frog step, the current transition dynamics T does not satisfy **constraints**$(\pi^*(T))$ or the leap frog integration terminates outside the feasible region, it is immediately rejected. This ensures that each sample satisfies the ϵ-ball property for each state $s \in \mathcal{D}$. Such "cleanup step" step is needed in case the leap frog integration stop when the position vector is outside of the constraints and did not have time to "roll-back" into the feasible region.

Algorithm 3: HMC with reflection for Bayesian ITL

1: First momentum half step
2: $m \leftarrow m - \frac{1}{2}\alpha\nabla E(w)$
3: **for** $l = 0$ to L **do**
4:    Full spatial step
5:    $w \leftarrow w + \alpha m$
6:    Transform w into T
7:    $T \leftarrow$ w_to_T(w)
8:    Create $\widehat{\pi}_\epsilon(\cdot \mid \cdot; T^*)$ with proposed T
9:    Squeeze maximum info
10:    $\pi \leftarrow \pi^*(T^{(i)})$
11:    Check for **constraints**(π) (See)
12:    **if** all **constraints**(π) satisfied **then**
13:        Full momentum step
14:        $m \leftarrow m - \alpha\nabla E(w)$
15:    **else**
16:        Bounce
17:        **constraints**(π) c is violated
18:        $\hat{n} \leftarrow \nabla c(T)/\|\nabla c(T)\|$
19:        $m \leftarrow m - 2(m \cdot \hat{n})\hat{n}$
20:    **end if**
21: **end for**
22: Full spatial step
23: $w \leftarrow w + \alpha m$
24: Last momentum half step
25: $m \leftarrow m - \frac{1}{2}\alpha\nabla E(w)$

Synthetic Environments

Gridworld Environment

The Gridworld environment is structured as follows:

- **Grid Size**: The world is a grid consisting of 5×5 tiles, resulting in a total of 25 distinct states.

- **Actions**: At each state, an agent can choose from four possible actions: move right, move up, move left, or move down.

- **Initial State**: The agent always starts from the bottom left corner of the grid, which is designated as the initial state.

- **Goal State**: The objective for the agent is to reach the goal state, located at the top right corner of the grid.

- **Dynamics**:

    - **Intended Actions**: When the agent selects an action, there is an 80% chance that it will move deterministically to the intended adjacent state.

    - **Slipping**: There is a 20% chance that the agent will slip, leading to a non-deterministic outcome. In such cases, the agent might end up in any one of the four neighboring tiles (right, left, up, down) of the intended state.

    - **Wall Interactions**: If an action would result in the agent moving into a wall (the edge of the grid), the agent remains in its current state. This mechanic ensures that the agent does not leave the confines of the grid.

The definition of the reward R in the grid world environment is structured as follows:

- **Soft-Wall Penalty**: If the agent attempts to move across a tile designated as a *soft-wall*, it incurs a penalty of -5 reward points for each attempt. This mechanic discourages the agent from crossing these specific tiles.

- **Movement Penalty**: For every other tile that the agent moves through, it receives a minor penalty of -0.1 reward points. This encourages the agent to find the shortest possible path to the goal.

- **Goal Reward**: Upon successfully reaching the goal state, the agent is awarded $+10$ reward points. This substantial reward signifies the completion of the episode and serves as the primary incentive for the agent to navigate the grid efficiently.

Reward function of Gridworld
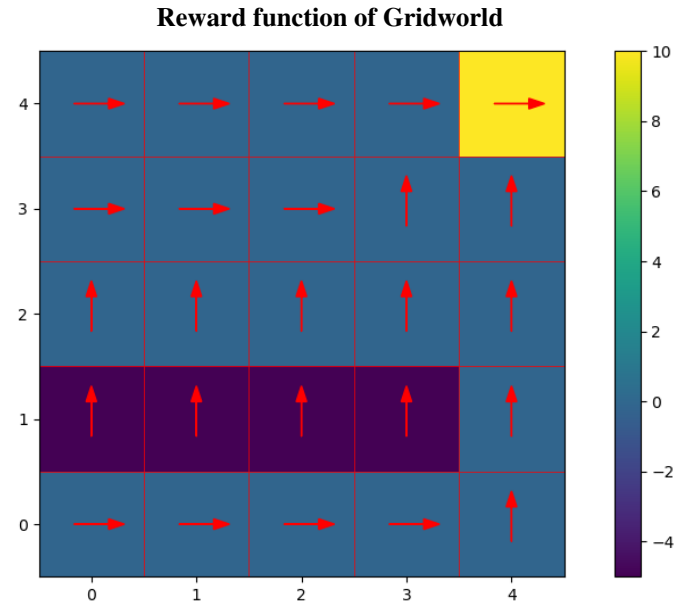
Figure 5: Visualization of the grid world environment. Each square in the 5x5 grid represents a unique state, colored based on the associated reward. The 'soft-wall' tiles are distinctively colored to represent a reward of -5. Red arrows on each tile indicate the direction of the optimal policy from that state, leading towards the goal state at the top right corner, which is marked in a different color and has a reward of 10. The starting point is at the bottom left corner, from where the arrows guide the optimal path through the grid.

This reward structure is designed to balance the objective of reaching the goal state as quickly as possible with the challenge of navigating around soft-wall tiles. The penalties for unnecessary movements and soft-wall crossings ensure that the agent must carefully consider each action, while the reward for reaching the goal state motivates the agent to complete its objective efficiently. Figure 5 shows the grid world environment, showcasing both the rewards for each state and the optimal policy indicated by red arrows. This environment presents a challenge for an agent to learn the most efficient path from the initial state to the goal state, taking into account the probabilistic nature of movement due to slipping. The deterministic and non-deterministic outcomes necessitate strategic planning and adaptability in the agent's approach to navigating the grid.

Transfer Task   In the transfer task, we preserve the structure of the original grid world environment, with no alterations to the state space or action set. However, we introduce a significant change to the reward function: the location of the soft-wall is shifted, thereby altering the reward landscape. This modification necessitates the derivation of a new optimal policy that accounts for the updated rewards and navigates the agent from the initial state to the goal state via a different path. See Figure 6.

Reward function of Gridworld in Transfer Task
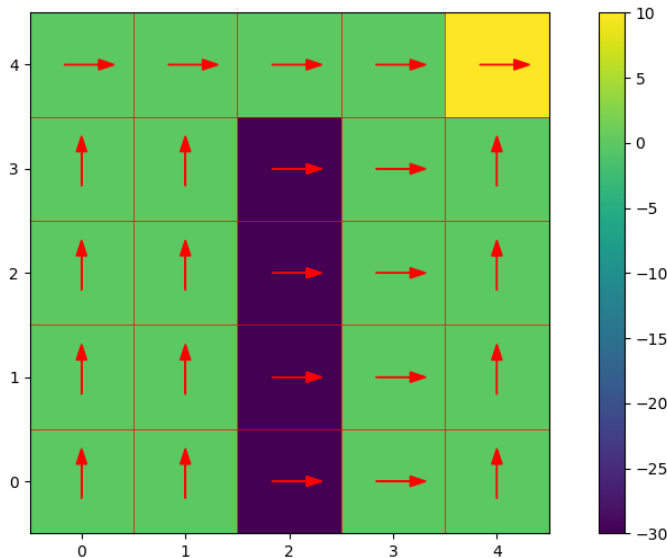
Figure 6: The grid world environment after the transfer task modification. The soft-wall tiles, previously located, have been repositioned, visibly changing the reward distribution across the grid. As a result, the optimal policy, indicated by red arrows, now follows a novel route that adapts to the new reward structure, aiming to minimize penalties and maximize returns en route to the goal state at the top right corner.

The updated reward function is defined identically to the original environment, with soft-wall tiles incurring a penalty of -5 reward points, other tiles a penalty of -0.1 points, and a reward of $+10$ points assigned upon reaching the goal

state. The shift in the soft-wall location directly affects the agent's trajectory, demonstrating the agent's ability to adjust its policy in response to changes in environmental dynamics. This transfer task effectively evaluates the flexibility and robustness of the learned policy.

Randomworld Environment

We introduce the RandomWorld environment (inspired by (Jiang et al. 2015)), which is designed to evaluate the performance of reinforcement learning algorithms under conditions of high uncertainty and stochasticity. The RandomWorld environment is characterized by the following properties:

- **State Space**: The environment comprises 15 distinct states.
- **State Space**: The environment comprises 5 distinct actions.
- **Dynamics** : For each state-action pair, 5 successor states are chosen at random to have nonzero transition probability. These probabilities are drawn independently from Uniform$[0, 1]$ and normalized to sum to one.
- **Initial State Distribution**: The initial state for each episode is selected with uniform probability across all 15 states.
- **Absence of a Goal State**: RandomWorld is devoid of a specified goal state, thus simulating scenarios where an agent's exploration is continuous and without a predetermined endpoint.
- **Reward Function**: Rewards are assigned randomly yet structured such that state 1 yields the highest expected reward, and state 15 the lowest. Specifically, the reward for state s, $R(s)$, is uniformly distributed within the interval $[16 - s - 1, 16 - s]$, aligning with the descending order of state desirability.

The inherent randomness in state transitions and rewards within RandomWorld poses a significant challenge to reinforcement learning strategies, necessitating the development of policies that are robust to uncertainty and variability in environmental dynamics.

Transfer Task   In the RandomWorld environment's transfer task, we introduce a modification to the reward function while preserving all other environmental characteristics. This adjustment is aimed at assessing the adaptability of reinforcement learning algorithms when confronted with a new reward paradigm. The specifics of the transfer task are as follows:

- **Inverted Reward Structure**: We reverse the ranking of state desirability; state 1 is now the least desirable state, and state 15 is the most desirable.
- **Random Reward Generation**: The reward for state s in the transfer task, $R_{\text{transfer}}(s)$, is determined by a random draw from a uniform distribution over the range $[s-1, s]$, thus ensuring that higher state numbers correspond to higher expected rewards.

This reversal in the reward hierarchy necessitates that the agent recalibrates its policy to align with the new set of rewards. It provides an insightful measure of the algorithm's capacity to adapt to drastic changes in the reward structure within a stochastic environment.

Generating batch data $\mathcal{D}$

A critical component of our experiments in offline reinforcement learning is the generation of a batch data $\mathcal{D}$, which is constructed based on a predefined coverage percentage of the state space and a given ϵ, measuring the degree of optimality of the expert $\pi_\epsilon(.|.;T^*)$ with respect to the true unknown dynamics T^*. The batch data $\mathcal{D}$ is created through the following procedure:

1. **State Selection**: We randomly select a certain percentage of the total states, corresponding to the coverage parameter, to include in our batch data.
2. **Action Selection**: For each state s included in our selection, we identify actions in the ϵ-ball $\epsilon(s;T^*)$, with respect to the ϵ-optimal expert $\pi_\epsilon(.|.;T^*)$.
3. **Transition Sampling**: We sample K transitions for each state-action pair (s,a) from the true dynamics T^*.
4. **Dataset Construction**: The batch dataset $\mathcal{D}$ is comprised of the transitions collected, each represented as a tuple (s,a,s'), with s as the state, a as the action, s' as the next state.

In our experimental setup, we define the value of K, which dictates the number of transitions sampled for each state-action pair that aligns with the ϵ-optimal expert policy $\pi_\epsilon(.|.;T^*)$. For the Gridworld environment, we set $K = 10$, acknowledging the larger state space and the need for a comprehensive dataset that encapsulates the dynamics around the optimal policy. In contrast, for RandomWorld, we set $K = 5$, suitable for its smaller size and complexity.

Averaging Procedure for Experimental Results

To achieve statistical rigor in our experiments, we average our results over multiple independently generated datasets for both Gridworld and RandomWorld environments:

- **Gridworld**: We generate 50 independent batch datasets for the Gridworld environment. The experimental results for each dataset are recorded, and the final result is obtained by averaging these outcomes.
- **RandomWorld**: For the RandomWorld environment, we create 20 independent instances of the environment. Each of these RandomWorld instances is accompanied by 5 independently generated batch datasets, leading to a total of 100 unique datasets (20 worlds multiplied by 5 datasets each). The experimental outcomes across these datasets are compiled, and their average is computed to determine the overall performance in the RandomWorld environment.

This methodology, involving the independent generation of each dataset and each world instance, provides a comprehensive and unbiased evaluation of the algorithms, ensuring that our results are not influenced by any specific configuration or sample of the environment.

Real-life ICU Environment

Following the experiments within a synthetic environments, we now transition to the evaluation of our methodology in a real-world scenario. To this end, we selected the Medical Information Mart for Intensive Care IV (MIMIC-IV) dataset as our experimental field. This dataset offers a rich, diverse, and challenging setting for testing our method, especially given its potential to contribute to advancements in healthcare analytics and patient care strategies.

About MIMIC-IV Dataset

The MIMIC-IV dataset, developed by the MIT Lab for Computational Physiology and publicly available, aggregates a vast range of anonymized health data from critical care units at Beth Israel Deaconess Medical Center in Boston. Covering over a decade's worth of patient admissions, it provides detailed records on demographics, vital signs, lab tests, medications, and more, establishing itself as a critical resource for healthcare model development. Its comprehensive scope spans all patient care aspects, enabling the creation of holistic models for predicting diverse patient outcomes. The dataset's richness lies in its variety, covering over 40,000 patients of different ages, ethnicities, and conditions, and its granularity, offering high-resolution data points and time-stamped records, which are essential for developing precise, dynamic healthcare models. Moreover, MIMIC-IV's public accessibility fosters a global research community's collaboration, enhancing healthcare analytics advancements.

Utilizing the MIMIC-IV dataset, we showcase out the learning applicability of our method in real-world healthcare, to get valuable insights from the data in such a complicated environemnt.

Data Preprocessing for Hypotension Analysis

In our investigation into hypotension within ICU settings, we tailored our preprocessing steps to exclusively include patients affected by this condition. Our methodology commenced with the application of specific filters on the MIMIC-IV dataset to accurately identify the patient cohort of interest. These filters were designed to capture adults aged 18 to 80 years, who had ICU stays of a minimum duration of 24 hours, and exhibited Mean Arterial Pressure (MAP) readings of 65mmHg or below, indicative of acute hypotension.

The analytical framework of our study is built around a carefully selected set of five clinical variables that constitute the state space, namely: creatinine levels (**(Crea)**), Glasgow Coma Scale score (**(GCS)**), mean blood pressure (**(BP)**), and the ration of partial pressure of oxygen, over fraction of inspired oxygen (**(O2)**). The action space encompasses two primary treatment modalities: intravenous (IV) fluid bolus therapy and vasopressor therapy. This precise filtering approach yielded a dataset comprising 1,684 distinct ICU admissions, from which we derived approximately 100,000 tuples (state, action, next_state) $\in \mathcal{D}$. This dataset serves as the foundation to evaluate our method and the baselines.

State Space Construction

The state space for our model is constructed by discretizing five key clinical variables extracted from the MIMIC-IV dataset: partial pressure of oxygen, fraction of inspired oxygen, mean blood pressure, Glasgow Coma Scale (GCS), and creatinine levels. Discretization involves binning these variables into distinct categories based on clinically relevant thresholds, as follows:

Based on the binning schema presented, the state space comprises all possible combinations of these bins, leading to a total of $3 \times 3 \times 2 \times 2 = 36$ unique states. This structure effectively captures diverse clinical scenarios within a manageable framework for analyzing the dynamics of hypotension treatment. To illustrate the discretization process and the resultant bin mapping, consider a hypothetical patient data point with the following clinical variable values:

- Partial Pressure of Oxygen / Fraction Inspired Oxygen: 150
- Mean Blood Pressure: 65 mmHg
- Glasgow Coma Scale: 10
- Creatinine: 5 mg/dL

Based on the discretization schema provided in Table 2, this patient data point would be mapped to the following bins:

- Partial Pressure of Oxygen / Fraction Inspired Oxygen (150): Bin 1 (since $100 \leq 150 < 200$)
- Mean Blood Pressure (65 mmHg): Bin 1 (since $65 < 70$ mmHg)
- Glasgow Coma Scale (GCS) (15): Bin 0 (since $10 \leq 12$)
- Creatinine (2.5 mg/dL): Bin 2 (since $5 \geq 4.9$)

Thus, the tuple $(150, 65, 15, 2.5)$ would be mapped to the discretized state $(1, 1, 0, 2)$ according to our binning process. This discretization approach allows us to capture a comprehensive yet manageable representation of the patient's clinical status, facilitating the application of our offline reinforcement learning model to infer the unknown dynamics T^*.

Action Space Definition

The action space in our model encapsulates the range of possible treatments administered to patients suffering from hypotension. It consists of four discrete actions, each representing a specific treatment strategy. The actions are enumerated as follows:

Each action is designed to reflect the clinical decisions made in the intensive care unit for managing patients' blood pressure levels. Action 0 (no treatment) represents a conservative approach, where no immediate intervention is applied. Action 1 (vasopressor therapy) and Action 2 (IV fluid bolus) correspond to the administration of specific treatments aimed at increasing blood pressure.

Reward Function Definition

The reward function, $R(s)$, quantifies the desirability of each state $x = (s_1, s_2, s_3, s_4)$ based on the bin values corresponding to the discretized clinical variables (each s_i correspond to a bin number). Formally, the reward function is defined as:

$$R(s) = 60 - 10 \times (s_1 + s_2 + s_4)$$

This formulation encapsulates our intuition that higher bin values for any of the clinical variables signify a deterioration in the patient's condition, indicating more severe or dangerous vital signs. Consequently, the reward decreases linearly by a factor of 10 for each increment in the bin values of the state components. The choice of this linear penalty ensures a straightforward interpretation of the state's severity, with a base reward of 60 being adjusted downward based on the sum of the bin values in the state.

While this reward function offers a reasonable approximation for assessing the clinical states in the context of hypotension, it is important to acknowledge that other formulations could be equally valid. The essential criterion for any chosen reward function is its ability to accurately differentiate between clinically favorable and unfavorable states, thereby guiding the reinforcement learning model towards optimizing treatment strategies that mitigate the risks associated with hypotension.

Transfer Task and Modified Reward Function

We introduce a transfer task to evaluate the model's adaptability and performance under a different reward function and keeping evrything else identical. The modified reward function for the transfer task is defined as:

$$R_{\text{transfer}}(s) = 60 - 10 \times (s_2 + s_4)$$

This adjustment means that the reward now decreases quadratically, rather than linearly, with the values of the features within each state $s = (s_1, s_2, s_3, s_4)$. The quadratic penalty intensifies the impact of higher bin values, more aggressively penalizing states indicative of worsening patient conditions. This change aims to test the method's sensitivity and response to more severe deteriorations in the clinical variables, pushing the reinforcement learning algorithm to prioritize avoiding high-risk states with even greater emphasis. Such a modification in the reward function's structure is pivotal for assessing the robustness and flexibility of our method. It allows us to explore how different reward formulations can influence decision-making strategies in the context of medical treatment optimization, particularly under scenarios with escalating risks.

Construction of the ϵ-Optimal Expert Policy π_ϵ

In the absence of explicit knowledge about the true dynamics T^* governing the environment, our methodology for obtaining an estimate of the ϵ-optimal expert policy, $\widehat{\pi}_\epsilon(\cdot|\cdot; T^*)$, leverages the historical batch data $\mathcal{D}$ collected from the ICU. We define an action a to be valid for a state s if and only if action a was executed in at least 5% of the instances where state s was observed in $\mathcal{D}$. Actions not meeting this criterion are considered invalid for the state, reflecting an approach that filters actions based on their historical prevalence and relevance to specific states.

Leveraging domain knowledge within the critical care domain, we set the ϵ parameter to 5 for our experiments. This

Table 2: Discretization of Clinical Variables into Bins

Abbrev	Clinical Variable	Threshold	Bin Value
O2	Partial Pressure of Oxygen / Fraction Inspired Oxygen	≥ 200	0
O2	Partial Pressure of Oxygen / Fraction Inspired Oxygen	< 200 and ≥ 100	1
O2	Partial Pressure of Oxygen / Fraction Inspired Oxygen	< 100	2
BP	Mean Blood Pressure	≥ 70 mmHg	0
BP	Mean Blood Pressure	< 70 mmHg	1
GCS	Glasgow Coma Scale (GCS)	≤ 12	0
GCS	Glasgow Coma Scale (GCS)	> 14	1
Crea	Creatinine	≤ 1.9 mg/dL	0
Crea	Creatinine	> 1.9 and ≤ 4.9 mg/dL	1
Crea	Creatinine	> 4.9 mg/dL	2

Action	Description
0	No treatment administered
1	Vasopressor therapy administered
2	Intravenous (IV) fluid bolus administered
3	Both vasopressor therapy and IV fluid bolus

Table 3: Definition of Actions in the Treatment Strategy Space

parameter choice reflects a balance, aiming to capture the degree of optimality in the actions taken by medical professionals in the ICU, under the assumption that the most frequently taken actions represent a near-optimal strategy given the complex dynamics and uncertainties inherent in patient care. Our experimental results demonstrate non-significant changes across various ϵ values, suggesting that the selected ϵ-optimal policy robustly encapsulates the expert behavior within the dataset, without significant sensitivity to the exact ϵ threshold.

Results

We include in this section the full set of results for the synthetic worlds where we include expert with various degree of optimality leading to 20% and 0% of stochastic-policy states) as well as multiple ϵ values as well for the results with the real healthcare dataset.
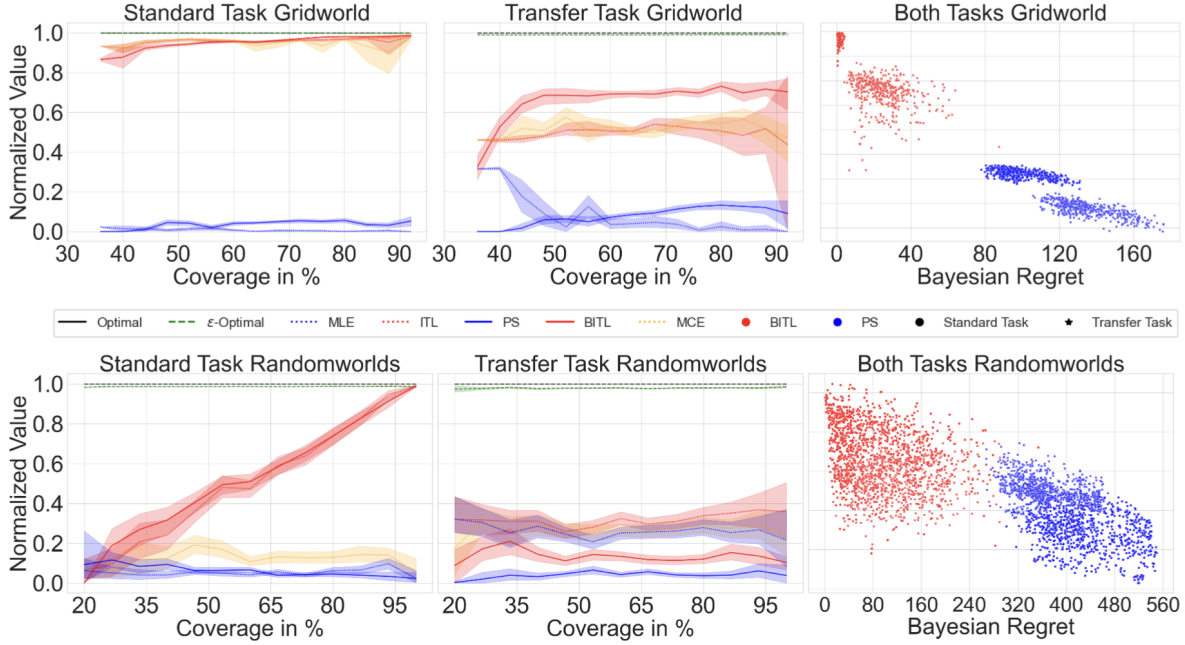
Figure 7: (40% stochastic-policy states) Top row: Normalized Value vs. Coverage for Gridworld (left: Standard Task, middle: Transfer Task), Bottom row: Normalized Value vs. Coverage for Randomworlds (left: Standard Task, middle: Transfer Task). Rightmost plots: Normalized Value vs. Bayesian Regret of both Tasks (top: Gridworld, bottom: Randomworlds).

Table 4: Gridworld and Randomworlds Results (40% stochastic-policy states)

| | Gridworld | | | | |
Method	MCE	BITL	ITL	MLE	PS
ϵ matching	0.65 ± 0.12	**0.78 ± 0.08**	0.65 ± 0.12	0.37 ± 0.06	0.38 ± 0.02
ϵ matching transfer	0.5 ± 0.11	**0.64 ± 0.08**	0.51 ± 0.11	0.39 ± 0.07	0.39 ± 0.02
Best matching	0.55 ± 0.11	**0.64 ± 0.08**	0.56 ± 0.11	0.31 ± 0.06	0.29 ± 0.02
Best matching transfer	0.45 ± 0.1	**0.54 ± 0.08**	0.45 ± 0.11	0.34 ± 0.07	0.31 ± 0.02
Time	117.47 ± 26.34	-	**0.32 ± 0.26**	-	-
Total Variation	137.62 ± 4.39	159.36 ± 3.98	**137.05 ± 4.32**	141.37 ± 3.8	160.05 ± 4.43
Value CVaR 1%	56.05 ± 15.08	**104.64 ± 5.43**	103.87 ± 15.67	-5.34 ± 0.54	-4.33 ± 1.68
Value CVaR 2%	76.7 ± 17.51	**107.36 ± 5.19**	106.46 ± 12.51	-5.18 ± 0.51	-3.49 ± 1.56
Value CVaR 5%	108.76 ± 26.54	109.04 ± 4.26	**109.7 ± 9.01**	-4.71 ± 0.47	-2.35 ± 1.35
Nbr constraints violated	3.06 ± 3.68	**0.0 ± 0.0**	**0.0 ± 0.0**	23.13 ± 6.59	16.37 ± 3.21
	Randomworlds				
Method	MCE	BITL	ITL	MLE	PS
ϵ matching	0.54 ± 0.12	0.75 ± 0.12	**0.76 ± 0.13**	0.43 ± 0.11	0.3 ± 0.05
ϵ matching transfer	0.46 ± 0.12	0.38 ± 0.1	**0.5 ± 0.13**	0.46 ± 0.12	0.31 ± 0.05
Best matching	0.38 ± 0.13	0.57 ± 0.12	**0.58 ± 0.15**	0.29 ± 0.11	0.19 ± 0.05
Best matching transfer	0.34 ± 0.13	0.26 ± 0.09	**0.37 ± 0.15**	0.34 ± 0.13	0.2 ± 0.05
Time	36.61 ± 26.36	-	**0.65 ± 0.39**	-	-
Total Variation	111.08 ± 2.42	123.3 ± 4.06	**102.02 ± 4.84**	111.07 ± 2.3	127.02 ± 2.66
Value CVaR 1%	-522.35 ± 5.49	-423.21 ± 29.84	**-404.02 ± 0.13**	-525.94 ± 3.86	-452.19 ± 22.88
Value CVaR 2%	-514.69 ± 7.06	-398.25 ± 30.3	**-397.26 ± 5.34**	-519.63 ± 6.42	-444.69 ± 20.16
Value CVaR 5%	-459.71 ± 23.48	-364.34 ± 34.06	**-366.43 ± 16.03**	-481.98 ± 23.31	-434.24 ± 17.22
Nbr constraints violated	11.81 ± 6.47	**0.0 ± 0.0**	**0.0 ± 0.0**	17.23 ± 6.75	11.66 ± 3.12
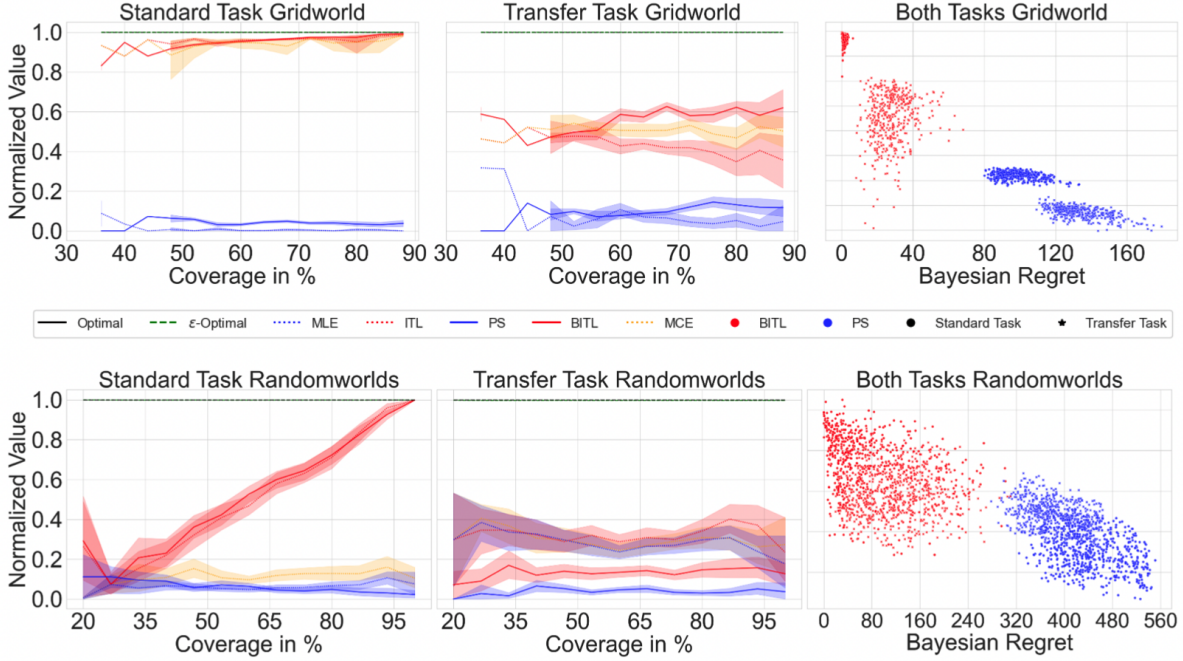
Figure 8: (20% stochastic-policy states) Top row: Normalized Value vs. Coverage for Gridworld (left: Standard Task, middle: Transfer Task), Bottom row: Normalized Value vs. Coverage for Randomworlds (left: Standard Task, middle: Transfer Task). Rightmost plots: Normalized Value vs. Bayesian Regret of both Tasks (top: Gridworld, bottom: Randomworlds).

Table 5: Comparison of Gridworld and Randomworlds (20% stochastic-policy states)

	Gridworld				
Method	MCE	BITL	ITL	MLE	PS
ϵ matching	0.64 ± 0.11	**0.74 ± 0.08**	0.64 ± 0.1	0.37 ± 0.06	0.32 ± 0.01
ϵ matching transfer	0.41 ± 0.06	**0.51 ± 0.05**	0.4 ± 0.06	0.32 ± 0.04	0.32 ± 0.01
Best matching	0.59 ± 0.11	**0.69 ± 0.08**	0.6 ± 0.1	0.34 ± 0.06	0.29 ± 0.02
Best matching transfer	0.4 ± 0.06	**0.5 ± 0.05**	0.39 ± 0.06	0.3 ± 0.04	0.31 ± 0.02
Time	114.66 ± 27.54	-	**0.75 ± 0.53**	-	-
Total Variation	**137.81 ± 3.79**	160.22 ± 3.89	138.71 ± 3.5	141.67 ± 3.11	160.4 ± 3.62
Value CVaR 1%	17.94 ± 7.28	**103.22 ± 7.96**	102.83 ± 33.76	-5.23 ± 0.56	-3.49 ± 0.56
Value CVaR 2%	54.96 ± 16.37	**106.6 ± 7.27**	104.7 ± 25.52	-5.04 ± 0.57	-2.9 ± 0.63
Value CVaR 5%	106.58 ± 42.1	**109.18 ± 5.81**	107.58 ± 16.89	-4.74 ± 0.5	-1.65 ± 0.92
Nbr constraints violated	0.82 ± 2.53	**0.0 ± 0.0**	**0.0 ± 0.0**	20.6 ± 5.73	14.19 ± 2.53

	Randomworlds				
Method	MCE	BITL	ITL	MLE	PS
ϵ matching	0.5 ± 0.13	0.72 ± 0.13	**0.73 ± 0.15**	0.38 ± 0.13	0.24 ± 0.05
ϵ matching transfer	0.42 ± 0.12	0.34 ± 0.11	**0.47 ± 0.13**	0.42 ± 0.12	0.25 ± 0.05
Best matching	0.45 ± 0.12	0.66 ± 0.13	**0.68 ± 0.15**	0.34 ± 0.12	0.21 ± 0.05
Best matching transfer	0.39 ± 0.13	0.31 ± 0.1	**0.43 ± 0.14**	0.39 ± 0.13	0.22 ± 0.05
Time	31.96 ± 25.36	-	**0.68 ± 0.69**	-	-
Total Variation	112.12 ± 2.43	124.38 ± 4.55	**103.32 ± 4.91**	112.07 ± 2.23	128.34 ± 2.51
Value CVaR 1%	-520.09 ± 1.89	**-401.79 ± 23.07**	-408.13 ± 0.14	-523.71 ± 1.51	-428.06 ± 0.79
Value CVaR 2%	-519.89 ± 1.72	**-388.77 ± 29.86**	-396.53 ± 5.59	-520.58 ± 1.96	-426.44 ± 1.25
Value CVaR 5%	-450.23 ± 25.6	-356.37 ± 33.32	**-352.47 ± 21.57**	-451.59 ± 23.83	-421.73 ± 2.52
Nbr constraints violated	7.03 ± 3.94	**0.0 ± 0.0**	**0.0 ± 0.0**	9.5 ± 3.95	9.22 ± 2.52
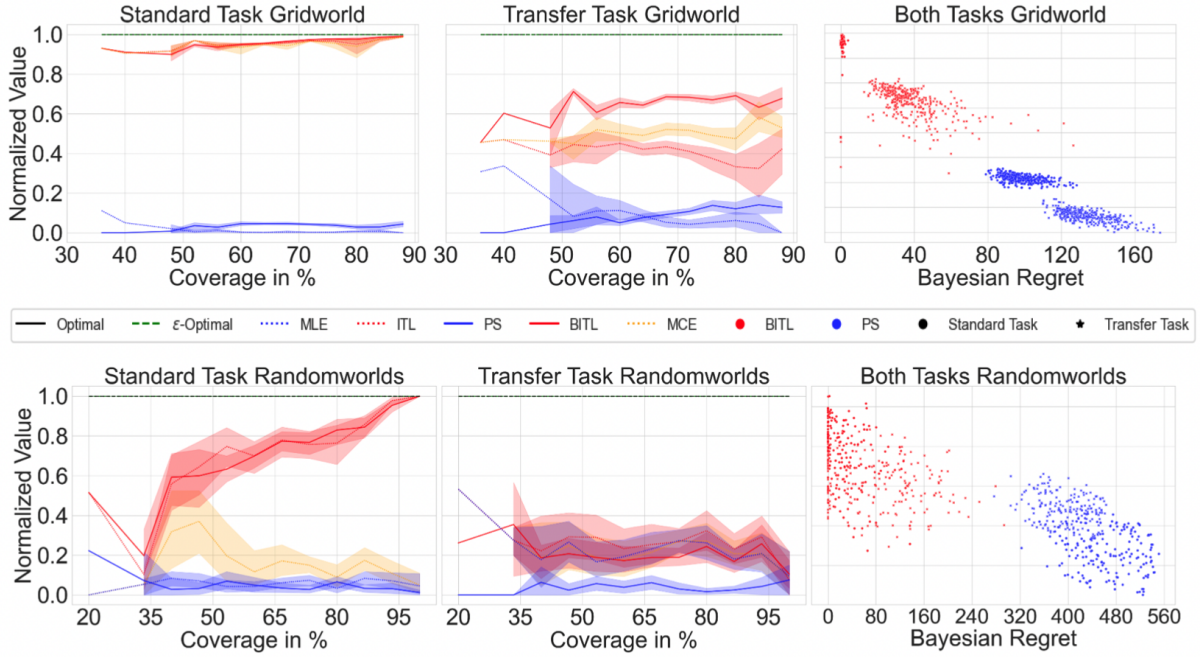
Figure 9: (0% stochastic-policy states) Top row: Normalized Value vs. Coverage for Gridworld (left: Standard Task, middle: Transfer Task), Bottom row: Normalized Value vs. Coverage for Randomworlds (left: Standard Task, middle: Transfer Task). Rightmost plots: Normalized Value vs. Bayesian Regret of both Tasks (top: Gridworld, bottom: Randomworlds).

Table 6: Comparison of Gridworld and Randomworlds (0% stochastic-policy states)

	Gridworld				
Method	MCE	BITL	ITL	MLE	PS
ϵ matching	0.68 ± 0.09	**0.75 ± 0.07**	0.68 ± 0.09	0.37 ± 0.06	0.29 ± 0.01
ϵ matching transfer	0.4 ± 0.06	**0.49 ± 0.05**	0.38 ± 0.06	0.29 ± 0.04	0.31 ± 0.01
Best matching	0.68 ± 0.09	**0.75 ± 0.07**	0.68 ± 0.09	0.37 ± 0.06	0.29 ± 0.01
Best matching transfer	0.4 ± 0.06	**0.49 ± 0.05**	0.38 ± 0.06	0.29 ± 0.04	0.31 ± 0.01
Time	119.86 ± 22.01	-	**4.36 ± 1.46**	-	-
Total Variation	**137.38 ± 3.3**	158.41 ± 3.37	138.6 ± 3.06	141.52 ± 2.55	160.22 ± 2.95
Value CVaR 1%	75.34 ± 19.3	**104.24 ± 7.94**	104.24 ± 37.65	-5.23 ± 0.48	-4.11 ± 0.22
Value CVaR 2%	102.59 ± 21.97	**108.18 ± 6.74**	105.64 ± 26.95	-5.2 ± 0.43	-3.65 ± 0.34
Value CVaR 5%	106.74 ± 23.68	**110.83 ± 5.93**	108.95 ± 18.49	-4.94 ± 0.35	-1.88 ± 0.84
Nbr constraints violated	0.08 ± 0.59	**0.0 ± 0.0**	**0.0 ± 0.0**	22.4 ± 5.23	13.15 ± 1.83
	Randomworlds				
Method	MCE	BITL	ITL	MLE	PS
ϵ matching	0.46 ± 0.13	0.77 ± 0.14	**0.78 ± 0.15**	0.32 ± 0.13	0.19 ± 0.05
ϵ matching transfer	0.37 ± 0.14	0.34 ± 0.13	**0.39 ± 0.16**	0.36 ± 0.15	0.23 ± 0.05
Best matching	0.46 ± 0.13	0.77 ± 0.14	**0.78 ± 0.15**	0.32 ± 0.13	0.19 ± 0.05
Best matching transfer	0.37 ± 0.14	0.34 ± 0.13	**0.39 ± 0.16**	0.36 ± 0.15	0.23 ± 0.05
Time	32.11 ± 27.16	-	**0.91 ± 0.55**	-	-
Total Variation	111.47 ± 2.27	117.66 ± 11.76	**101.44 ± 2.87**	111.84 ± 2.26	128.14 ± 2.54
Value CVaR 1%	-520.09 ± 3.18	**-343.11 ± 0.56**	-350.2 ± 11.25	-521.78 ± 0.0	-428.28 ± 0.05
Value CVaR 2%	-517.71 ± 2.71	**-278.91 ± 36.29**	-343.9 ± 20.59	-520.09 ± 2.39	-427.96 ± 0.4
Value CVaR 5%	-446.29 ± 4.08	**-246.36 ± 41.54**	-254.84 ± 47.72	-447.26 ± 3.11	-425.21 ± 1.24
Nbr constraints violated	4.9 ± 1.71	**0.0 ± 0.0**	**0.0 ± 0.0**	6.9 ± 1.91	8.59 ± 2.03

Table 7: Healthcare dataset results ($\epsilon = 10$)

Method	Standard Task					Transfer Task				
	MLE	ITL	MCE	BITL	PS	MLE	ITL	MCE	BITL	PS
Best matching	0.33	**0.47**	0.38	0.46	0.31	0.34	**0.50**	0.10	0.47	0.34
ϵ matching	0.52	**1**	0.68	**1**	0.51	0.58	**0.94**	0.16	**0.94**	0.58
Nbr Constraints	49	**0**	43	**0**	52	-	-	-	-	-
Time	-	**2.31**	180	-	-	-	-	-	-	-
Bayesian Regret	-	-	-	**0.55**	10	-	-	-	**0.44**	5.40

Table 8: Healthcare dataset results ($\epsilon = 15$)

Method	Standard Task					Transfer Task				
	MLE	ITL	MCE	BITL	PS	MLE	ITL	MCE	BITL	PS
Best matching	0.33	**0.48**	0.25	0.49	0.31	0.34	**0.47**	0.15	**0.47**	0.34
ϵ matching	0.52	**1**	0.43	**1**	0.51	0.58	**0.97**	0.31	**0.97**	0.58
Nbr Constraints	49	**0**	51	**0**	52	-	-	-	-	-
Time	-	**1.78**	94	-	-	-	-	-	-	-
Bayesian Regret	-	-	-	**1.02**	10	-	-	-	**0.56**	5.40